AIAA JOURNAL
Vol. 36, No. 5, May 1998

Prediction of the High-Reynolds-Number Flow over a Two-Dimensional Bump

Xiaohua Wu* and Kyle D. Squires†
Arizona State University, Tempe, Arizona 85287-6106

Large eddy simulation (LES) has been applied to prediction of the high-Reynolds-number boundary layer flowing over a bump. Approximate boundary conditions were used in the LES to model the wall layer in which the instantaneous wall stress is correlated with the velocity at the first layer of grid points. Two formulations of the approximate boundary conditions were employed. In the first formulation, a constrained relation was used in which the mean wall shear stress is specified a priori either from experimental measurements or from a separate solution of the Reynolds-averaged Navier–Stokes (RANS) equations. In the second formulation, an unconstrained relation, which is based on an instantaneous power-law velocity profile, was used. Calculations were also performed in which the wall stress was computed directly, i.e., as if the near-wall flow were resolved. In the region resolved by the LES, the strong distortions of the mean flow, streamwise fluctuations, and turbulent shear stress are reasonably well predicted, and the relatively rapid recovery downstream of the trailing edge is also captured. However, neither LES nor RANS reproduces the plateau in skin friction measured upstream of the bump summit (attributed to early relaminarization in the experiments). LES predictions of the mean flow and turbulence intensities using the dynamic eddy viscosity model are relatively insensitive to the particular formulation of approximate boundary conditions. However, in calculations without a subgrid model, LES predictions exhibit large errors compared to experiments, and the quantitative levels of such errors are also sensitive to the choice of wall-layer model.

I. Introduction

LARGE eddy simulation (LES) is a predictive technique that has undergone significant advancement. One of the principal improvements in advancing LES as a viable means for the prediction of complex turbulent flows has been development of dynamic subgrid-scale (SGS) models.[1] Dynamic models have been applied in a number of flows, yielding satisfactory predictions compared to experiments or results from direct simulations.[1–11] Because of the high computational cost required to adequately resolve near-wall structures when no-slip boundary conditions are applied, the majority of previous calculations have been restricted to flows at low to moderate Reynolds numbers. Consequently, LES of high-Reynolds-number, complex flows is an area currently under intensive development.[12,13]

One of the key issues that must be addressed in applying LES to high-Reynolds-number flows is the treatment of the boundary conditions on solid surfaces. Although the cost of Reynolds-averaged computations is not strongly dependent on the Reynolds number, the need to adequately resolve near-wall structures in boundary layers imposes an increasingly stringent computational cost in LES, e.g., resolution requirements in the viscous sublayer grow almost quadratically with Reynolds number.[14] One approach to circumventing the restriction to moderate Reynolds numbers is through the use of wall-layer models. In this approach, rather than applying no-slip boundary conditions on the velocity, the effect of the wall is indirectly imposed on the LES through the instantaneous wall shear stress. The wall stress is in turn supplied by a set of approximate boundary conditions.

Current approximate boundary conditions are based on the assumption that there is a weak interaction between the modeled near-wall layer and the resolved outer region. The near-wall flow can then be interpreted as a Stokes layer driven by the outer core flow. The coupling between the wall model and LES under this assumption then occurs locally via the velocity or pressure gradient inside the flow at the first layer of LES grid points nearest the wall. Simple boundary conditions can be derived for equilibrium flows by further assuming that the dynamics of the near-wall layer are universal and that the velocity obeys a prescribed log or power law.[15,16] More sophisticated approaches do not require that the near-wall velocity satisfy a given profile but still require weak interaction between the wall region and outer part of the boundary layer. An equilibrium assumption is also introduced, and a reduced set (boundary layer) of equations is solved to calculate the wall stress.[12,13] Equilibrium-based wall-layer models have yielded accurate predictions in fully developed flows, e.g., between plane channels or in a square duct.

Measurements in many complex flows show that universal, e.g., log-law, velocity profiles may not exist.[17] Further, in boundary layers approaching separation, boundary conditions that require wall-normal distance in terms of wall units, as in the log law, can become singular. Extension of LES to the high Reynolds numbers of engineering interest will likely require improvements of existing methods or the development of new wall-layer models altogether. An important step toward developing improved treatments of the wall layer is the evaluation of existing approaches in complex nonequilibrium flows. Therefore, the primary objective of this study is the evaluation of some existing approaches in a nontrivial complex boundary layer and the establishment of an important baseline on which further improvements can be made.

As discussed in greater detail in Sec. II.B, an alternative to prescribing a log- or power-law profile as part of the wall-layer model can be based on an a priori prescription of the mean wall shear stress in formulation of the approximate boundary conditions. The mean stress is obtained using either experimental measurements or a separate Reynolds-averaged Navier–Stokes (RANS) calculation. The drawback of this approach, of course, is that the calculation requires input of this important quantity and that the LES itself does not predict the mean friction. In addition, for cases in which the skin friction is provided via a separate mean-flow calculation, a reliable RANS model is needed. In this regard, recent progress has been reported concerning several aspects of Reynolds-averaged models.[18–22] Relevant to this work is the v^2–f model developed by Durbin.[23] The model is an appropriate candidate for prescribing the mean friction in an approximate boundary condition for LES because it does not require the use of ad hoc damping functions near the wall, and previous applications have yielded reasonable predictions of a range of flows.[23–25] Thus, although the mean friction is not

Received Feb. 10, 1997; revision received Dec. 1, 1997; accepted for publication Jan. 10, 1998. Copyright © 1998 by the American Institute of Aeronautics and Astronautics, Inc. All rights reserved.

*Faculty Research Associate, Department of Mechanical and Aerospace Engineering, Box 876106.

†Associate Professor, Department of Mechanical and Aerospace Engineering, Box 876106.

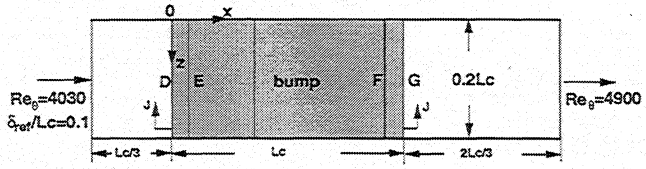

Fig. 1a Top view of the computational domain.

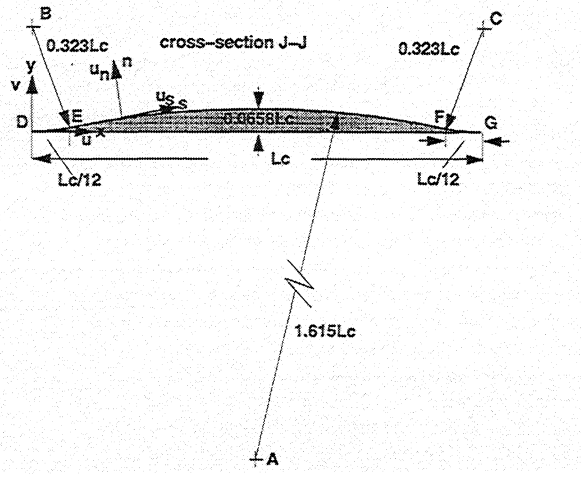

Fig. 1b Bump dimensions; D, E, F, and G tangent points; upstream concave surface $0 \le x/L_c \le 1/12$; convex surface $1/12 \le x/L_c \le 11/12$; and downstream concave surface $11/12 \le x/L_c \le 1$.

predicted, the incorporation of an external prescription of the mean wall stress into the LES does permit one to examine the behavior of the computation away from the wall (resolved by the LES) and to gain some insight into the sensitivity of LES predictions to various prescriptions of the wall shear.

The particular flow considered in this work is the turbulent boundary layer flowing over a bump. The bump is formed by a prolonged convex surface with two additional short concave regions fore and aft (Fig. 1). A canonical zero-pressure-gradient boundary layer at a momentum thickness Reynolds number $Re_{\theta,\mathrm{ref}} = 4030$ is introduced one-third chord length upstream of the onset of curvature. (The ref subscript is used throughout to denote quantities measured at the inflow location.) The boundary layer then experiences three sign changes in streamwise pressure gradient and four sign changes in surface curvature. The particular configuration shown in Fig. 1 is considered because the boundary-layer properties have been reported by Webster et al.[17] and provide a means for evaluating simulation results.

LES calculations and experimental measurements at lower Reynolds numbers have shown that, corresponding to the abrupt changes in pressure gradient and surface curvature near the leading and trailing edges of the bump, the boundary layer forms two internal layers within which shear generation and dissipation of turbulence kinetic energy are nearly balanced and are large compared with those in other parts of the flow.[11,17] Boundary-layer properties exhibit a strong departure from equilibrium over the rear surface of the bump (downstream of the summit) and are significantly different from their profiles upstream of the summit. An interesting feature of the flow is that along the trailing flat plate both the mean flow and turbulence quantities exhibit a relatively rapid return to equilibrium. Each of these features provides a significant challenge to predictive methods. In this study, LES predictions using existing equilibrium-based, wall-layer models are evaluated at higher Reynolds numbers than considered in previous work. As described in greater detail in Sec. II.B, the mean wall shear is input to some of the approximate boundary conditions using the experimental measurements of Webster et al.[17] or from a v^2–f RANS computation. Whereas the main purpose of the auxiliary RANS calculation is to provide the mean wall shear for the approximate boundary condition in the LES, it is also of interest to compare RANS predictions of the flowfield to the experimental data. Therefore, a complete overview of both the LES and RANS is provided in the next section. Comparisons of simulation results with the experimental measurements and evaluations of the approximate boundary conditions are given in Sec. III, followed by a summary and conclusions in Sec. IV.

II. Background

A. Simulation Overview for RANS

Time or ensemble averaging the equations of mass and momentum conservation yields the RANS equations

$$\mathrm{div}\langle \boldsymbol{u} \rangle = 0 \tag{1}$$

$$\frac{\partial \langle \boldsymbol{u} \rangle}{\partial t} + \mathrm{div}[\langle \boldsymbol{u} \rangle \langle \boldsymbol{u} \rangle] = -\mathrm{grad}\langle p \rangle + \mathrm{div}\left\{ \left(\frac{1}{Re} + \nu_t \right) [\mathrm{grad}\langle \boldsymbol{u} \rangle + (\mathrm{grad}\langle \boldsymbol{u} \rangle)^{\mathcal{T}}] \right\} \tag{2}$$

A gradient transport hypothesis has been used to close the Reynolds stress, where ν_t is the turbulent eddy viscosity (the $\mathcal{T}$ superscript denotes the transpose). In Eqs. (1) and (2), $\langle \boldsymbol{u} \rangle$ is the mean velocity vector whose Cartesian components are $(\langle u \rangle, \langle v \rangle)$. In the RANS calculation the full form of Eq. (2) is solved for both the $\langle u \rangle$ and $\langle v \rangle$ components, i.e., the boundary-layer approximation is not made. Thus, important variations in the flow, e.g., the pressure gradient in the wall-normal direction, are not neglected. Velocities in Eqs. (1) and (2) are normalized by the inflow freestream value U_{ref} and lengths by the bump height h, and $Re = U_{\mathrm{ref}} h/\nu$, where ν is the kinematic viscosity. The turbulent eddy viscosity ν_t is

$$\nu_t = C_\mu \langle v'^2 \rangle T \tag{3}$$

where T is the timescale defined as

$$T = \max\left[\frac{K}{\varepsilon}, 6\left(\frac{\nu}{\varepsilon} \right)^{\frac{1}{2}} \right] \tag{4}$$

The turbulence kinetic energy K, dissipation rate ε, and wall-normal fluctuations $\langle v'^2 \rangle$ appearing in Eqs. (3) and (4) are obtained through the following transport equations[23]:

$$\frac{\partial K}{\partial t} + \mathrm{div}[\langle \boldsymbol{u} \rangle K] = \mathcal{P} - \varepsilon + \mathrm{div}\left\{ \left(\frac{1}{Re} + \frac{\nu_t}{\sigma_K} \right) \mathrm{grad}\, K \right\} \tag{5}$$

$$\frac{\partial \varepsilon}{\partial t} + \mathrm{div}[\langle \boldsymbol{u} \rangle \varepsilon] = \frac{C_{\varepsilon 1}\mathcal{P} - C_{\varepsilon 2}\varepsilon}{T} + \mathrm{div}\left\{ \left(\frac{1}{Re} + \frac{\nu_t}{\sigma_\varepsilon} \right) \mathrm{grad}\, \varepsilon \right\} \tag{6}$$

$$\frac{\partial \langle v'^2 \rangle}{\partial t} + \mathrm{div}[\langle \boldsymbol{u} \rangle \langle v'^2 \rangle] = K f_{22} - \langle v'^2 \rangle \frac{\varepsilon}{K} + \mathrm{div}\left\{ \left(\frac{1}{Re} + \frac{\nu_t}{\sigma_K} \right) \mathrm{grad}\langle v'^2 \rangle \right\} \tag{7}$$

where f_{22} appearing in Eq. (7) is evaluated from

$$\frac{\partial f_{22}}{\partial t} = -(1 - C_1)\frac{2/3 - \langle v'^2 \rangle / K}{T} + C_2 \frac{\mathcal{P}}{K} - f_{22} + C_L^2 l^2 \,\mathrm{div}(\mathrm{grad} f_{22}) \tag{8}$$

Note the use of a pseudotime-derivative term in Eq. (8) so that the transport equations possess the same structure for numerical convenience, i.e., the left-hand side of Eq. (8) vanishes at convergence. The rate of turbulence kinetic energy production and the length scale l are given by

$$\mathcal{P} = \nu_t [\mathrm{grad}\langle \boldsymbol{u} \rangle + (\mathrm{grad}\langle \boldsymbol{u} \rangle)^{\mathcal{T}}] \mathrm{grad}\langle \boldsymbol{u} \rangle$$
$$l^2 = \max\left[\frac{K^3}{\varepsilon^2}, C_3^2 \left(\frac{\nu^3}{\varepsilon} \right)^{\frac{1}{2}} \right] \tag{9}$$

Model constants appearing in Eqs. (3–9) are the same as those in Ref. 23, i.e.,

$$C_\mu = 0.19, \quad C_{\varepsilon 1} = 1.3 + 0.25/[1 + (n/2l)^2]^4, \quad C_{\varepsilon 2} = 1.9$$
$$C_1 = 1.4, \quad C_2 = 0.3, \quad C_L = 0.3$$
$$C_3 = 70, \quad \sigma_K = 1.0, \quad \sigma_\varepsilon = 1.3$$

The origin of the streamwise coordinate x is at the onset of curvature (Fig. 1). The bump chord/height ratio (L_c/h) is 15.2:1. The

height of the computational domain is $2/3L_c$ measured from the flat plate ($y = 0$). The length of the upstream and downstream flat plates are $1/3L_c$ and $2/3L_c$, respectively. A streamline-normal coordinate system (s, n) was also used with the n-axis perpendicular to the lower surface (Fig. 1).

No-slip conditions were applied on the wall for the velocity components. For K, ε, $\langle v'^2\rangle$, and f_{22}, the boundary conditions on solid surfaces are

$$K_w = 0, \qquad \varepsilon_w = \frac{2\nu K_{n\to 0}}{n^2_{\to 0}} \tag{10}$$

$$\langle v'^2\rangle_w = 0, \qquad f_{22,w} = \frac{-20\nu^2\langle v'^2\rangle_{n\to 0}}{n^4_{\to 0}\varepsilon_w} \tag{11}$$

At the inflow boundary, the mean velocity, turbulence kinetic energy, and wall-normal fluctuations were prescribed through interpolation of the experimental measurements of Webster et al.[17] To obtain the profiles of ε and f_{22} at the inlet, a separate precomputation of a flat plate boundary layer at $Re_\theta = 4030$ was performed. In the precomputation, only the values of ε and f_{22} were allowed to fluctuate, whereas all other quantities were fixed to their interpolated profiles. At the exit plane, a convective boundary condition was used together with a correction on the streamwise velocity to ensure global mass conservation.[26] Streamwise derivatives of K, ε, $\langle v'^2\rangle$, and f_{22} were assumed to be zero at the exit. Over the top surface of the computational domain $\partial\langle u\rangle/\partial y = 0$, $\langle v\rangle = 0$ were applied, whereas the derivatives of K, ε, $\langle v'^2\rangle$, and f_{22} along the y direction were assumed to be zero.

The numerical method used to solve the momentum and continuity equations (1) and (2) is the fractional step method in generalized coordinates.[27,28] The computational domain is transformed from the Cartesian (x, y, z) system to a body-fitted curvilinear nonorthogonal system (ξ, η, z), where ξ is the streamwise coordinate and η is the coordinate normal to the flat plate. The dependent variable is transformed from $\langle \boldsymbol{u}\rangle$ to a volume flux vector using area vectors. Transport equations for K, ε, $\langle v'^2\rangle$, and f_{22} were solved using successive overrelaxation. At each time step, Eqs. (5) and (6) and (7) and (8) were iterated sequentially as two coupled systems until the maximum residuals were reduced to machine zero.

The grids were constructed so that the coordinate lines of constant ξ were perpendicular to the flat plate $y = 0$ and top surface of the computational domain. The grids were stretched only along the y direction. The grid size used in the RANS calculation was 181×101. Based on the friction velocity at the inlet, this corresponds to a spatial resolution $\Delta x^+ = 180$. The first grid point normal to the wall was within one wall unit.

Using the inlet profile as the initial condition, the system of Eqs. (1) and (2) and (5–8) was advanced to steady state. The flow was considered converged when the following criteria were satisfied:

$$\max\left\{\frac{|\langle u\rangle(x,y,t) - \langle u\rangle(x,y,t - 10\delta_{\text{ref}}/U_{\text{ref}})|}{U_{\text{ref}}}\right\} < 10^{-5} \tag{12}$$

$$\max\left\{\frac{|\langle v\rangle(x,y,t) - \langle v\rangle(x,y,t - 10\delta_{\text{ref}}/U_{\text{ref}})|}{U_{\text{ref}}}\right\} < 10^{-6} \tag{13}$$

$$\max\left\{\frac{|K(x,y,t) - K(x,y,t - 10\delta_{\text{ref}}/U_{\text{ref}})|}{U^2_{\text{ref}}}\right\} < 10^{-6} \tag{14}$$

$$\max\left\{\frac{|\langle v'^2\rangle(x,y,t) - \langle v'^2\rangle(x,y,t - 10\delta_{\text{ref}}/U_{\text{ref}})|}{U^2_{\text{ref}}}\right\} < 10^{-6} \tag{15}$$

B. Simulation Overview for LES

In LES, mass and momentum conservation is enforced for the large-scale resolved variables, which are obtained by filtering the Navier–Stokes equations

$$\operatorname{div}\bar{\boldsymbol{u}} = 0 \tag{16}$$

$$\frac{\partial\bar{\boldsymbol{u}}}{\partial t} + \operatorname{div}(\bar{\boldsymbol{u}}\bar{\boldsymbol{u}}) = -\operatorname{grad}\bar{p} + \operatorname{div}\left\{\left(\frac{1}{Re} + \nu_{\text{SGS}}\right)[\operatorname{grad}\bar{\boldsymbol{u}} + (\operatorname{grad}\bar{\boldsymbol{u}})^T]\right\} + \mathcal{E}_c \tag{17}$$

where ν_{SGS} is the SGS eddy viscosity. In Eqs. (16) and (17) an overbar denotes the filtered variable. The term $\mathcal{E}_c$ appearing in Eq. (17) is the commutation error because, in general, the filtering operation does not commute with differentiation. As shown in Ref. 29, the commutation error is second order in the filter width. For calculation of spatial derivatives using approximations that are second-order accurate, as in the present work, filtering can be assumed to commute with differentiation (see Ref. 29 for further discussion).

The eddy viscosity in Eq. (17) is expressed as[4]

$$\nu_{\text{SGS}} = C\bar{\Delta}^2|\bar{S}|, \qquad \boldsymbol{S} = [\operatorname{grad}\bar{\boldsymbol{u}} + (\operatorname{grad}\bar{\boldsymbol{u}})^T]/2 \tag{18}$$

Following Germano et al.,[1] a second filter, the test filter (denoted using $\hat{\cdot}$), is used to derive an expression for the model coefficient C

$$C = -\frac{1}{2}\frac{L_{ij}M_{ij}}{M_{ij}M_{ij}} \tag{19}$$

where

$$M_{ij} = \hat{\bar{\Delta}}^2|\hat{\bar{S}}|\hat{\bar{S}}_{ij} - \bar{\Delta}^2\widehat{|\bar{S}|\bar{S}_{ij}}, \qquad L_{ij} = \widehat{\bar{u}_i\bar{u}_j} - \hat{\bar{u}}_i\hat{\bar{u}}_j \tag{20}$$

where the least-squares approach of Lilly[30] has been used to obtain Eq. (19). The filter widths at the subgrid and subtest levels are denoted by $\bar{\Delta}$ and $\hat{\bar{\Delta}}$, respectively.

In the results presented in this paper, the model coefficient is calculated by averaging the numerator and denominator in Eq. (19) over the homogeneous spanwise direction to eliminate numerical instabilities arising from small values of the denominator. Therefore, the coefficient C is time dependent and a function of the two inhomogeneous coordinates. A clipping function was used to ensure nonnegative values of C following the spanwise averaging applied to Eq. (19). The test filtering operation was performed in physical space on the coordinate plane $\eta = \text{const}$ using a top-hat filter of width equal to two mesh spacings. Test filtering was performed numerically by applying Simpson's rule of integration.

In the LES, a time-dependent velocity field at the inflow boundary was obtained through a separate precalculation of a canonical flat plate boundary layer over a continuous momentum thickness Reynolds number range $3900 \le Re_\theta \le 4500$. The method used for generating the time-dependent turbulent inflow condition is a modification of the multiple scale analysis of Spalart.[31] The streamwise length of the domain for the precomputation is $15\delta_{\text{ref}}$. The grid resolution and other dimensions are the same as those in the bump simulation (see Refs. 32 and 33 for further discussion). After a statistically steady state had been achieved, the three velocity components at a streamwise station $Re_\theta = 4030$ were stored for $300\delta_{\text{ref}}/U_{\text{ref}}$ at a time step $dt = 0.01\delta_{\text{ref}}/U_{\text{ref}}$ and were subsequently fed to the inlet ($x/L_c = -1/3$) of the spatially developing bump flow simulation. As in the experiments of Webster et al.,[17] the inlet boundary-layer thickness $\delta_{\text{ref}} = 1.5h$. Boundary conditions applied on the top and exit planes were essentially similar to those described in Sec. II.A for the RANS calculation. Periodic boundary conditions were applied in the spanwise direction, which has a width of $L_c/5$.

The region $0 \le y^+_{\text{ref}} \le 25$ was modeled using approximate boundary conditions in which the instantaneous wall shear stress is correlated with the LES velocity near the wall, i.e., at the first layer of grid points away from the wall.[15,16] Two formulations for computing the instantaneous wall stress in the streamwise, $\tau_{s,w}$, and spanwise, $\tau_{z,w}$, directions are used; these calculations are subsequently referred to as LES1 and LES2.

In LES1, a simple relation is used in which the instantaneous wall stress is constrained through prescription of the mean value, i.e.,

$$\tau_{s,w} = \frac{\bar{u}_{s,2}(x,y,z,t)}{\langle\bar{u}_{s,2}\rangle(x,y,t)}\langle\tau_{s,w}\rangle, \qquad \tau_{z,w} = \nu\frac{\bar{u}_{z,2}(x,y,z,t)}{n_2} \tag{21}$$

where subscripts s and z denote corresponding streamwise and spanwise components in the wall-normal coordinate system shown in Fig. 1. Subscript 2 refers to the first layer of pressure grid points away from the wall. Note that the application of Eq. (21) requires specification of the mean stress $\langle\tau_{s,w}\rangle$. In LES1, $\langle\tau_{s,w}\rangle$ was prescribed through interpolation of the experimental data of Webster et al.[17] To examine the sensitivity of LES predictions to the specific prescription of $\langle\tau_{s,w}\rangle$, a simulation was also performed in which

the mean shear was obtained from the RANS predictions described in the preceding section. This second calculation is referred to as LES1R in Sec. III. Finally, note that the mean velocity $\langle \bar{u}_s \rangle (x, y, t)$ appearing in Eq. (21) is obtained by spanwise averaging at each time step during the computation. In LES2, an unconstrained formulation was used, i.e., approximate boundary conditions were implemented in which the mean skin friction is predicted in the LES. The specific wall model used in LES2 is that from Werner and Wengle.[34] In this approach, the local and time-dependent, near-wall velocity profile is fit to a power-law profile, i.e.,

$$\tau_{s,w} = \nu \frac{\bar{u}_{s,2}}{n_2} \quad \text{if} \quad |\bar{u}_{s,2}| < \frac{\nu}{4n_2} A^{2/(1-B)}, \qquad A = 8.3, \qquad B = \tfrac{1}{7}$$

$$= \frac{\bar{u}_{s,2}}{|\bar{u}_{s,2}|} \left\{ \frac{1-B}{2} A^{(1+B)/(1-B)} \left(\frac{\nu}{2n_2} \right)^{1+B} + \frac{1+B}{A} \left(\frac{\nu}{2n_2} \right)^{B} |\bar{u}_{s,2}| \right\}^{2/(1+B)} \quad \text{otherwise} \tag{22}$$

Note that, by construction, LES1 (and LES1R) using Eq. (21) do not yield a direct prediction of the mean skin friction because this quantity is prescribed a priori using experimental measurements or RANS results. The instantaneous wall stress is constrained by the prescribed mean value as well as through the mean velocity near the wall. The variation in the shear stress occurs through the instantaneous LES velocity along the first layer of grid points. The advantage of this approach is that it circumvents the need to assume that the near-wall flow satisfies an equilibrium profile. Because of the need to specify the mean wall stress, LES predictions using Eq. (21) are not fully predictive. However, calculations using the approximate boundary conditions (21) are useful for examining the sensitivity of LES predictions to prescription of the mean wall shear. Compared to the constrained formulation, Eq. (22) used in LES2 does not require prescription of the mean wall shear stress and does permit an independent calculation of the skin friction. Prediction of the mean friction is achieved at the expense of assuming the existence of an instantaneous power-law velocity profile. Note also that the boundary condition (22) is unconstrained in the sense that the instantaneous shear stress is more strongly dependent on the instantaneous velocity along the first layer of grid points than in Eq. (21). Errors in prediction of the near-wall LES velocity should in turn be expected to have a larger adverse effect on simulations performed using Eq. (22) as compared to Eq. (21).

For both formulations, i.e., LES1 and LES2, an additional set of simulations were performed in which no subgrid model was employed. Previous work at moderate Reynolds numbers has shown that the overall effect of the SGS model is not large. Calculations with and without the subgrid model in the flow over the bump will help clarify the role of the SGS model at higher Reynolds numbers. The calculations without the subgrid model corresponding to LES1 and LES2 are referred to in the next section as LES1no and LES2no, respectively. Finally, to further test the sensitivity of LES predictions to perturbations in the approximate boundary conditions, a calculation, referred to as LES3, was undertaken in which the instantaneous wall shear stress is evaluated directly from the LES velocity gradient, i.e., as if the near-wall flow had been directly resolved:

$$\tau_{s,w} = \nu \frac{\bar{u}_{s,2}(x, y, z, t)}{n_2}, \qquad \tau_{z,w} = \nu \frac{\bar{u}_{z,2}(x, y, z, t)}{n_2} \tag{23}$$

The application of Eq. (23) is equivalent to the application of a strong perturbation to the wall-layer model and provides a gauge of LES performance under an apparently erroneous approximate boundary condition. An important distinction between LES3 and the other LES calculations is that the approximate boundary conditions used in LES1, LES1R, and LES2, although requiring considerable empiricisim, do not suffer from the same type of error as Eq. (23).

The numerical methodology adopted to solve the momentum and continuity equations (16) and (17) is the same as that described in Sec. II.A. The results were obtained using a grid of $361 \times 51 \times 33$ in the streamwise, wall-normal, and spanwise directions, respectively. Based on the friction velocity at the inlet, this corresponds to a spatial resolution of $\Delta x^+ = 90$, $\Delta y^+_{\min} > 25$, and $\Delta z^+ = 70$. Using the inlet profile at $t = 0$ as the initial condition, the flow was allowed to evolve for $100\delta_{\text{ref}}/U_{\text{ref}}$ at a time step $dt = 0.01\delta_{\text{ref}}/U_{\text{ref}}$, and statistics were then collected for a period of $200\delta_{\text{ref}}/U_{\text{ref}}$.

III. Results

The surface static pressure coefficient C_{pw} $[=(\langle \bar{p}_w \rangle - \langle \bar{p}_{w,\text{ref}} \rangle)/\frac{1}{2}U^2_{\text{ref}}]$ is compared with the experimental measurements of Webster et al.[17] in Fig. 2a. Figure 2a shows that the streamwise pressure gradient undergoes quasistep changes near the bump leading and trailing edge, where surface curvature also changes sign. The combination of perturbations in both pressure gradient and curvature is a common feature for boundary layers developing over streamlined bodies and substantially complicates downstream development.[17,35,36] Compared with experiments, the RANS prediction of C_{pw} is accurate, with a maximum error less than $5\%|C_{pw}|_{\max}$. Note that the upper computational boundary is the same distance from the lower test surface as the upper wall in the experiments of Webster et al.[17] No-slip boundary conditions on the upper computational boundary, however, were not applied in the calculations (see Sec. II.A). Durbin performed an independent v^2–f calculation using the same (two-dimensional) geometry as in the experiment and in which the no-slip boundary condition on the upper wall was also applied, obtaining a similar pressure coefficient as in the present RANS prediction.

Figure 2a shows that LES2 predictions of C_{pw} are accurate downstream of the bump leading edge ($x/L_c > 0$), with a similar error as in the RANS calculation. At the leading edge, Fig. 2a also shows that C_{pw} is overpredicted in LES2. The upper-wall boundary conditions used in the RANS and LES were essentially the same, and the overprediction in the LES is unlikely the effect of the boundary conditions. Errors from boundary conditions would manifest themselves throughout the domain rather than in isolated regions of the flow. The slight overprediction near $x = 0$ occurs at least partly because in the LES the near-wall flow is not resolved. The pressure used for the calculation of C_{pw} is that along the first layer of grid points nearest, but not at, the wall. Correcting for the wall-normal variation would presumably improve the agreement, especially in the region of adverse pressure gradient near the leading edge. For further discussion of issues related to the prediction of quantities such as the pressure coefficient, see Ref. 37. Finally, Fig. 2a also shows that LES predictions using the approximate boundary conditions (21) (LES1 and LES1R) are very similar to that from LES2 except

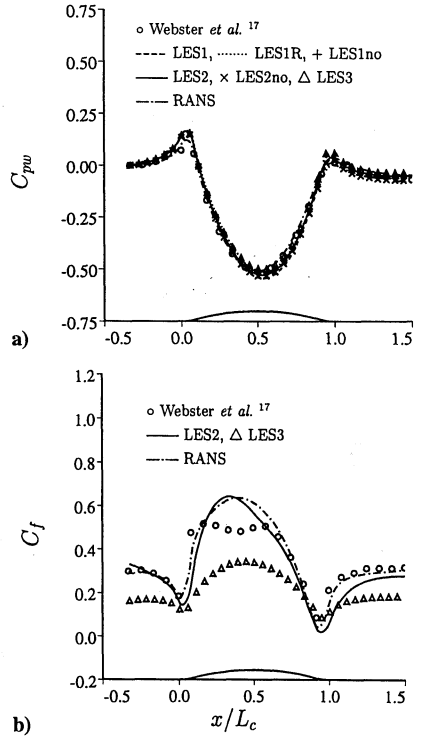

Fig. 2 Wall-static pressure coefficient and skin-friction coefficient: a) C_{pw} and b) C_f.

near the summit. Without the SGS model (LES1no and LES2no), there is a relatively small effect on C_{pw}, with a slight overprediction at the summit and trailing edge.

Skin friction from the calculations are compared to those of Webster et al.[17] in Fig. 2b. The RANS prediction is accurate upstream of the leading edge and downstream of $x/L_c = 0.7$. Compared to the measurements, the maximum error in these two regions is less than $5\%C_{f,\max}$. Near the bump summit, $0.2 < x/L_c < 0.7$, the skin-friction coefficient is less accurate. The dip/plateau in the experimental data upstream of the summit was attributed by Webster et al.[17] to the early stages of relaminarization. Figure 2b shows relatively large differences between the RANS calculation and measurements near the summit, showing the effects of possible relaminarization on the skin friction are not captured. Downstream of the trailing edge, the relatively rapid recovery of the skin friction is accurately captured by the RANS.

One possible explanation for the discrepancy between measurements and simulations in the prediction of C_f is due to the onset of three-dimensional effects, a subject of several studies in curved flows. Bandyopadhyay and Ahmed[36] acquired measurements in an S-shaped wind tunnel showing that spanwise nonuniformities in concave regions are correlated with the Görtler instability and that the growth of a corner vortex is accompanied by an increasing spanwise nonuniformity in the skin friction. Webster et al.[17] obtained measurements at various spanwise locations and verified spanwise uniformity. Based on the discussion in Ref. 17, the error in the RANS prediction of C_f is most likely due to the inability of the model to reproduce effects of boundary-layer relaminarization near the summit rather than due to the error in C_{pw} or three dimensionality.

Figure 2b shows that the skin friction predicted in LES2 using the power-law approximate boundary condition (22) is in relatively poor agreement with measurements. As in the RANS calculation, the plateau upstream of the bump summit is not captured. Along the surface of the bump downstream of the summit in the region of strong adverse pressure gradient, the skin friction is reasonably well predicted, an interesting result considering the crude nature of the boundary condition. In the recovery region downstream of the trailing edge, however, the wall-layer model (22) yields a slower recovery than measured. These features are one illustration of the shortcomings of current equilibrium-based wall-layer models when applied to prediction of strongly distorted boundary layers and should not be unexpected. These results further underscore the need for more accurate near-wall models. Nevertheless, it should be kept in mind that the wall shear stress calculated using Eq. (22) merely serves the purpose of closing the approximate boundary condition for the LES away from the wall ($y^+_{\text{ref}} > 25$). As will be shown in Figs. 3–7, the predicted mean velocity and second-order statistics in the flow away from the wall are relatively insensitive to the specific distribution of the wall shear stress appearing in the approximate boundary conditions and are also in reasonably good agreement with measurements. Figure 2b also shows the skin friction obtained in LES3 using the relation (23), which assumes that the near-wall region is resolved. As expected, C_f is substantially lower than the experimental values except near the trailing edge, where the flow is on the verge of separation. Note that such a strong perturbation does not have a measurable effect on C_{pw} (cf. Fig. 2a), indicating that C_{pw} is determined primarily by the overall flow configuration.

Profiles of the mean horizontal velocity $\langle\bar{u}\rangle$ at four streamwise locations are compared with the experimental measurements of Webster et al.[17] in Fig. 3. The first station ($x/L_c = -1/3$) is at the inflow boundary, and the next three stations are on the downstream side of the bump. (Aside from the inlet, no measurements were made upstream of the bump summit.) The velocity profiles are normalized by the local edge velocity U_e, which is defined as the maximum along each vertical traverse.[17] The vertical coordinate is normalized by the corresponding boundary thickness δ_{U_e}. At the inflow boundary, the LES precomputation used to generate the inflow signal yields a mean profile in very good agreement with the measurements. As mentioned in Sec. II.A, inflow profiles in the RANS calculation were prescribed from the measurements. Over the entire downstream side of the bump, the agreement between LES predictions and experiments is excellent, indicating that, in the region resolved by the LES, i.e., $y^+_{\text{ref}} > 25$, the simulation accurately captures the strong departure and return to equilibrium in the mean flow.

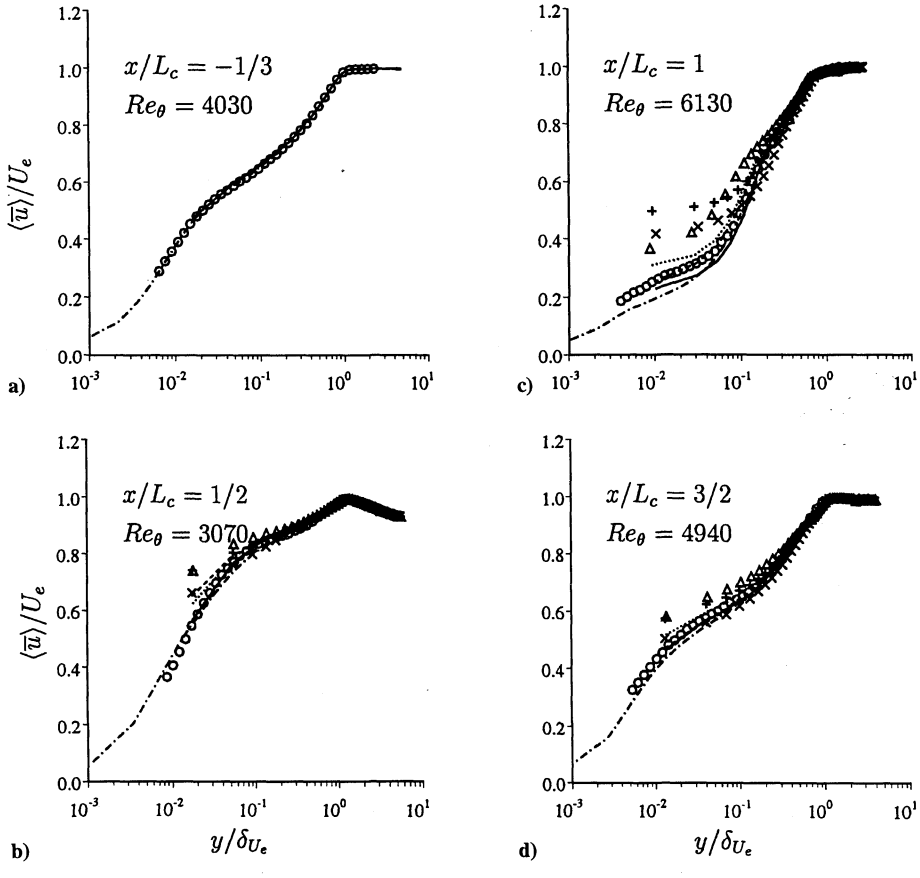

Fig. 3 Mean velocity $\langle\bar{u}\rangle/U_e$: ○, Webster et al.[17]; – – –, LES1; · · · ·, LES1R; +, LES1no; ——, LES2; ×, LES2no; △, LES3; and — · —, RANS.

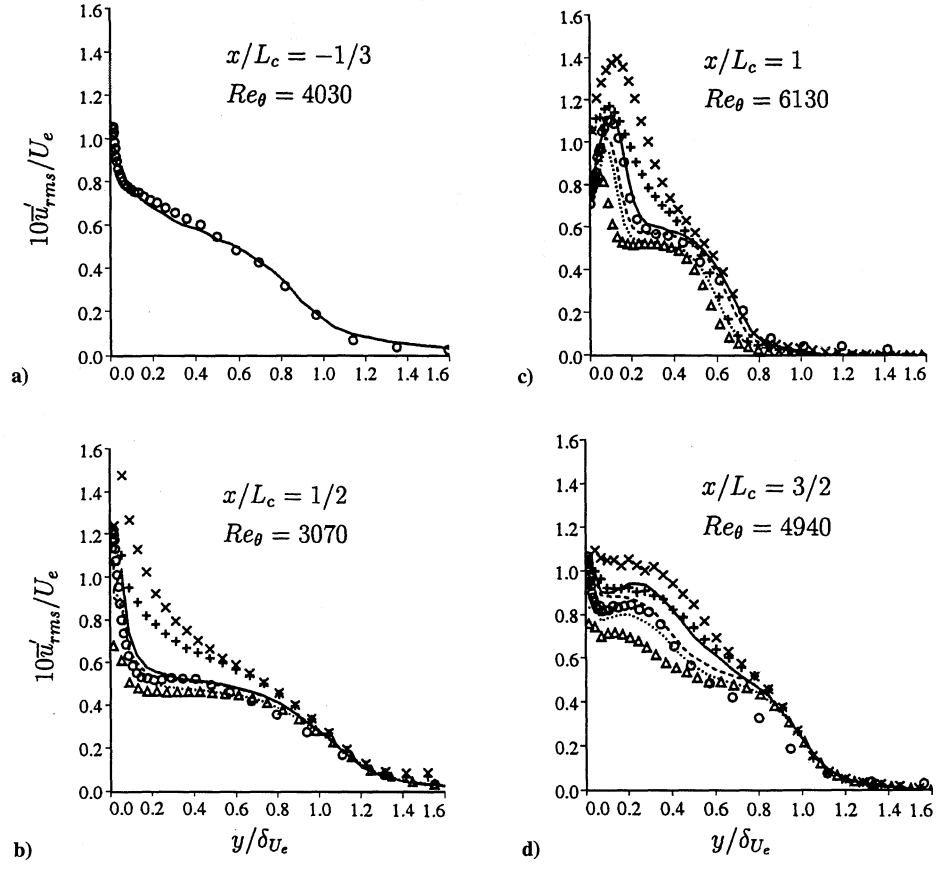

Fig. 4 Horizontal turbulence intensity $\bar{u}'_{\rm rms}/U_e$: ○, Webster et al.[17]; – – –, LES1; - - - -, LES1R; +, LES1no; ——, LES2; ×, LES2no; and △, LES3.

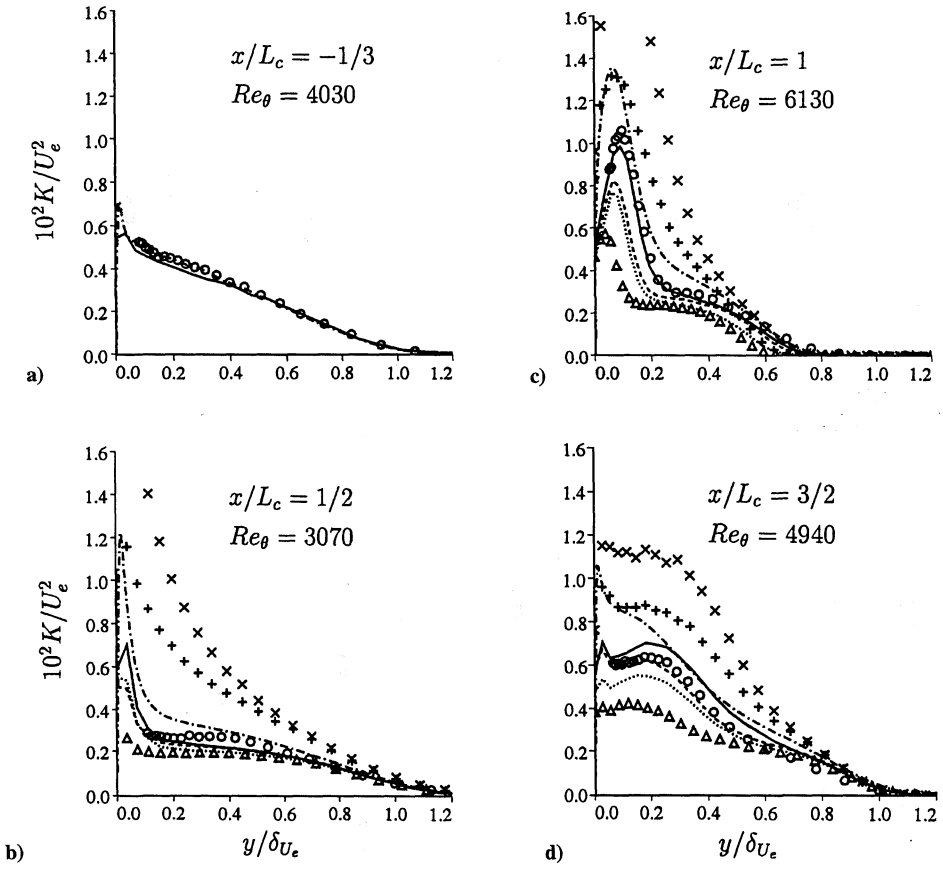

Fig. 5 Turbulence kinetic energy: ○, Webster et al.[17]; – – –, LES1; - - - -, LES1R; +, LES1no; ——, LES2; ×, LES2no; △, LES3; and —·—, RANS.

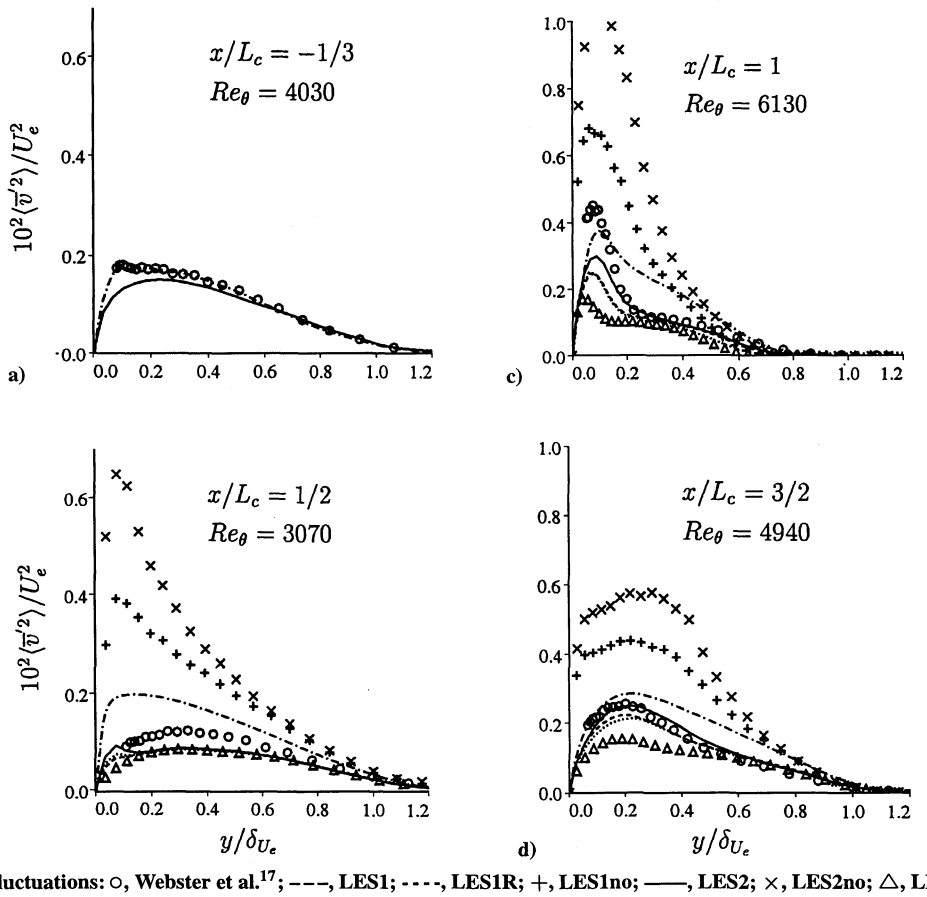

Fig. 6 Wall-normal fluctuations: ○, Webster et al.[17]; – – –, LES1; - - - -, LES1R; +, LES1no; ——, LES2; ×, LES2no; △, LES3; and —·—, RANS.

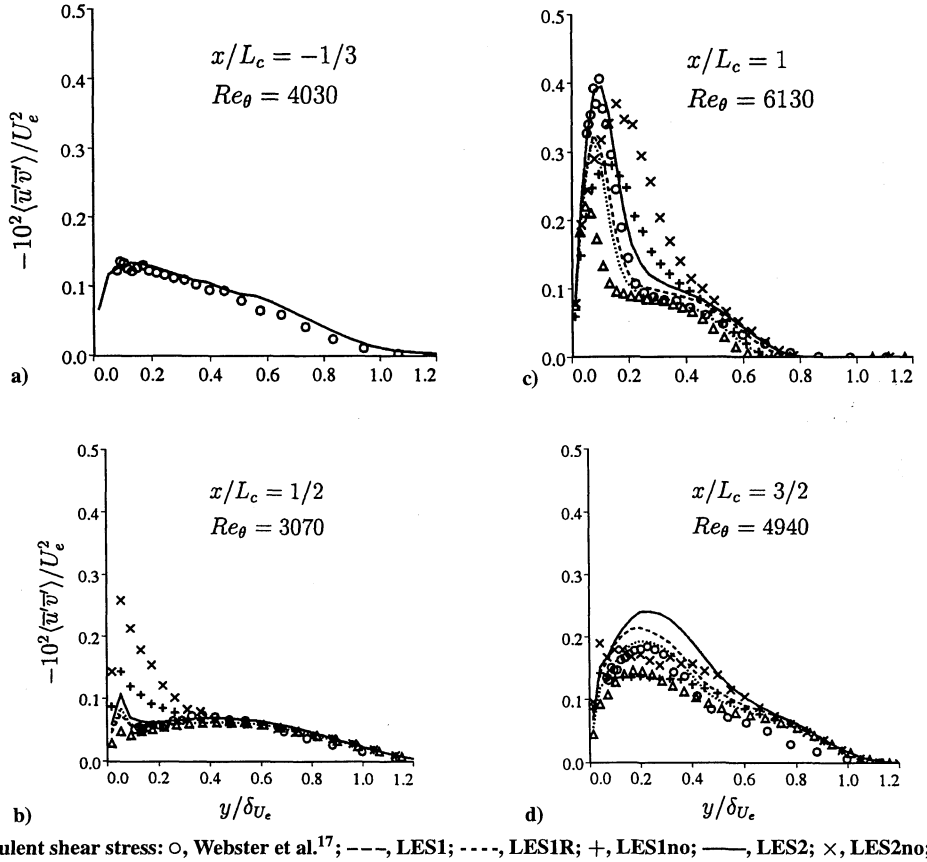

Fig. 7 Turbulent shear stress: ○, Webster et al.[17]; – – –, LES1; - - - -, LES1R; +, LES1no; ——, LES2; ×, LES2no; and △, LES3.

It is further interesting to note that the small differences among LES1, LES1R, and LES2 predictions indicate that the mean velocity away from the wall is relatively insensitive to prescription of the wall shear stress from the approximate boundary condition. Previous work in similar flows has shown that the boundary layer outside a thin inner equilibrium region (roughly one to two momentum thicknesses) is driven by the outer irrotational flow.[38] The outer irrotational flow is dictated by the streamwise pressure gradient and curvature, which in turn are determined by the overall flow configuration. Thus, the assumption of weak inner/outer layer interaction discussed in Sec. I is approximately valid in the present flow over the bump. Consequently, one might expect a priori that the outer flow resolved in the LES should not be particularly sensitive to details of the inner region, consistent with the results in Fig. 3. Another interesting feature apparent in Figs. 3b–3d is the behavior of the mean velocity predicted in calculations with no subgrid model. Though LES1, LES1R, and LES2, obtained using the dynamic model, are in good agreement with measurements, the near-wall mean profiles predicted in LES1no and LES2no, where no SGS model is used, are much larger than the measured mean velocity. LES3 predictions of the mean velocity using the approximate boundary condition (23) are inaccurate, even though the dynamic model is still employed. In addition, the predictions are somewhat worse than those obtained in LES1no and LES2no. Figure 3 also shows that the v^2–f model accurately reproduces the distortion and relaxation of the mean velocity distribution as the flow passes the bump. At the summit, the RANS prediction of the mean flow has a maximum error less than 3% of the freestream velocity. At the trailing edge, RANS predictions are accurate beyond $0.05\delta_{U_e}$, whereas along the trailing flat plate ($x/L_c = 3/2$) the prediction is also accurate, capturing the rapid return to equilibrium in the mean flow.

LES predictions of the horizontal turbulence intensity are compared with experiments in Fig. 4. At the summit, LES1, LES1R, and LES2 all yield accurate predictions of $\tilde{u}'_{\text{rms}}$. At the trailing edge, LES2 predictions are still quite accurate; the peaks in LES1 and LES1R are slightly below the data. Over the trailing flat plate ($x/L_c = 3/2$), the maximum errors for LES1, LES1R, and LES2 are less than 10% of the peak fluctuation level. The results in Fig. 4 also show that the SGS model has a rather large effect on the streamwise fluctuations. Without the dynamic model (LES1no and LES2no), $\tilde{u}'_{\text{rms}}$ are significantly overpredicted. This is interesting because, in calculations at moderate Reynolds numbers where the near-wall flow is resolved rather than modeled, the effect of SGS model is less significant.[11] This is consistent with the finer resolution needed in calculations that resolve near-wall structures, in turn limiting the contribution of unresolved motions. In addition, the perturbation applied to the flow in LES3 through use of inaccurate approximate boundary conditions results in about a 20% drop in the streamwise intensity. Also interesting is that the no-model results in Fig. 4 show a greater sensitivity of the turbulence fluctuations in the outer flow resolved by LES to errors in the wall-layer models. LES2no predictions, in which the near-wall instantaneous velocity satisfies a power law, are substantially larger than experimental measurements, compared to LES1no in which the wall stress is specified using Eq. (21) and constrained by the mean wall shear.

Predictions of the turbulence kinetic energy are compared with the experimental measurements in Fig. 5. As shown in Fig. 5a, results from the LES precomputation used to generate the inflow condition ($x/L_c = 1/3$) are in good agreement with the experimental measurements. At the bump summit, the LES correctly predicts the knee in the profile of the kinetic energy (Fig. 5b), which results from the development of an internal layer over the upstream convex surface.[11,17] LES results at $x/L_c = 1/2$ are below the data at $0.4\delta_{U_e}$, whereas the RANS prediction yields larger kinetic energy between $0.1\delta_{U_e}$ and $0.3\delta_{U_e}$. At the trailing edge, both the LES and RANS predictions capture the outward shift in the peak turbulence kinetic energy, which is typical in turbulent boundary layers experiencing strong adverse pressure gradient.[35,39]

In the near-wall region at $x/L_c = 1$, LES2 predictions are accurate, whereas LES1 and LES1R underpredict the peak value. The peak in K is also overpredicted in RANS. Over the trailing flat plate ($x/L_c = 3/2$), LES1, LES1R, and LES2 accurately capture the rapid return to equilibrium in the kinetic energy, whereas Fig. 5d shows that K is overpredicted in the RANS calculation. Similar to the streamwise intensity, turbulence kinetic energy profiles from the LES3 prediction are lower than the experimental measurements. Without the SGS model (LES1no and LES2no), the turbulence kinetic energy is not accurate, again demonstrating the significant role of the model at higher Reynolds numbers. The relatively large differences between LES1no and LES2no also show that errors in K predicted in calculations without the SGS model reflect a stronger coupling between the approximate boundary conditions and outer LES using the unconstrained wall-layer model (22). This is consistent with the discussion in Sec. II.B that errors in prediction of the near-wall LES velocity should have a larger adverse affect on simulations performed using Eq. (22), as compared to Eq. (21).

Predictions of the turbulent normal stress $\langle\tilde{v}'^2\rangle$ are compared to those of Webster et al.[17] in Fig. 6. Figure 6a shows that the wall-normal fluctuations yielded from the LES precomputation used to generate the inflow condition are in reasonable agreement with that measured by Webster et al.[17] but below the data, especially close to the wall. One reason for the discrepancy is that the profile shown in Fig. 6a is the resolved component of the normal stress, i.e., the subgrid contribution is not included. In addition, the underprediction of the wall-normal fluctuations is typical in LES of wall-bounded flows and due to the inability of the computation (both the grid and subgrid model) to completely capture component anisotropy near the wall. Figure 6b shows that, at the summit, LES1, LES1R, and LES2 predictions of the peak are smaller, whereas the RANS result is larger than the measurements. The disagreement between RANS predictions and measurements, however, should not be considered so serious in this case because v^2 provides the velocity scale in the v^2–f model and may not necessarily be interpreted as the wall-normal fluctuation, especially away from the wall. On the downstream side of the bump in the region of strong adverse pressure gradient, there is a significant increase in the wall-normal fluctuations near the wall. At $x/L_c = 1$, simulations underpredict the peak value. The lower values from the LES are again partly due to the inability to completely capture the anisotropy close to the wall as well as to fully resolve all of the energy content in the normal stresses. Over the downstream surface, LES and RANS predictions of the recovery in the wall-normal fluctuations are in good agreement with measurements. Figure 6 also shows that, for calculations without the SGS model (LES1no and LES2no), predictions of the normal stress $\langle\tilde{v}'^2\rangle$ are very poor and the model has an important role to play. Similar to the streamwise fluctuations and turbulence kinetic energy presented in Figs. 4 and 5, the wall-normal fluctuations in Fig. 6 exhibit larger errors for LES2no, using the unconstrained approximate boundary condition, as compared to LES1no, using the constrained formulation.

Profiles of the resolved turbulent shear stress from the LES are compared with the experimental measurements in Fig. 7. Figure 7a shows that the inflow profile matches the experimental data very well. At the summit, LES1, LES1R, and LES2 accurately capture the reduction in shear stress by convex curvature and the favorable pressure gradient. At the trailing edge, LES2 predictions of the shear stress are accurate, but LES1 and LES1R underpredict the peak value. Over the trailing flat plate at $x/L_c = 3/2$, LES results yield the location of the peak value, but the magnitude is overpredicted in LES1 and LES2, though the overprediction in LES1 is rather small. Consistent with the streamwise intensity, turbulence kinetic energy, and wall-normal fluctuations shown in Figs. 4–6, the resolved shear stress in LES3, in which the wall stress is computed from the very poor assumption that the near-wall flow is resolved, is underpredicted compared with the experimental data. However, the mismatch between LES and measurements in the second-order statistics is substantially moderate compared with the discrepancy in C_f shown in Fig. 2b. This again indicates that the outer LES for this particular flow is indeed quite insensitive to the specific prescription of the approximate boundary conditions. Without the SGS model, LES1no and LES2no predictions of the shear stress are significantly less accurate. Similar to the behavior of the turbulence intensities from simulations with no subgrid model, the constrained LES1no prediction of the shear stress exhibits a smaller error than the unconstrained LES2no (see Figs. 7b and 7c). Also note that, even though

the errors in Fig. 7d for LES2no are not significantly over the data downstream of the trailing edge, locations of the maximum shear stress are nevertheless missed.

IV. Summary

The performance of existing equilibrium-based approximate boundary conditions has been studied through the application of LES to the prediction of a well-defined, high-Reynolds-number, complex turbulent flow. The boundary conditions are based on the assumption that the instantaneous wall shear stress is correlated with the velocity near the wall. In the constrained formulation, the instantaneous wall shear stress fluctuates according to the probability density function of the streamwise velocity component in the first layer of LES grid points. The mean wall shear stress was supplied a priori using either the experimental measurements of Webster et al.[17] or a separate v^2–f prediction. In the unconstrained approach, prescription of the mean wall shear is not required. Instead, an explicit algebraic correlation between the instantaneous wall shear and the instantaneous velocity away from the wall is employed by fitting the local and time-dependent, near-wall velocity profile to a power-law profile.

Simulation results show that, together with the dynamic eddy viscosity model, the LES yields reasonable predictions of the mean velocity, streamwise turbulence intensity, and turbulent shear stress in the region resolved by the LES. It is interesting that the predictions obtained using the three different prescriptions of the mean wall shear stress in the approximate boundary conditions, i.e., one distribution identical to the experiments, one from the v^2–f calculation that differs from the experiments, and a profile (from the unconstrained formulation) that is in rather poor agreement with the experiments, yield relatively accurate descriptions of the outer flow. The insensitivity of LES predictions to the specific prescription of the mean wall shear is in turn consistent with earlier studies in similar flows showing that the boundary layer outside a thin inner (equilibrium) region is driven by the outer irrotational flow and, therefore, less affected by the shear stress.[38]

Simulation results obtained without the dynamic model show large overpredictions of the second-order statistics compared to measurements. Errors in calculations without the SGS model also reflect a stronger coupling between the wall-layer model and outer LES using the unconstrained boundary conditions in which the instantaneous shear stress is obtained through a presumed (instantaneous) power-law velocity profile. More sophisticated approaches that effectively constrain shear stress predictions, e.g., through incorporation of the mean stress, should be expected to be less sensitive to modeling errors in the SGS fluctuations.

Acknowledgments

The work is supported by the U.S. Office of Naval Research (Grants N00014-94-1-0047 and N00014-94-1-1053; Program Officer, L. Patrick Purtell). Most of the simulations were performed on the Cray C90s and T90 at the U.S. Department of Defense High Performance Computing Major Shared Resource Centers (Corps of Engineers Waterways Experiment Station and Naval Oceanographic Office). The authors gratefully acknowledge valuable discussions with P. A. Durbin, J. K. Eaton, T. S. Lund, D. R. Webster, and D. A. Degraaff.

References

[1]Germano, M., Piomelli, U., Moin, P., and Cabot, W. H., "A Dynamic Subgrid-Scale Eddy Viscosity Model," *Physics of Fluids A*, Vol. 3, No. 7, 1991, pp. 1760–1765.

[2]Moin, P., Squires, K. D., and Cabot, W., "A Dynamic Subgrid-Scale Model for Compressible Turbulence and Scalar Transport," *Physics of Fluids A*, Vol. 3, No. 11, 1991, pp. 2746–2757.

[3]Zang, Y., Street, R. L., and Koseff, J. R., "A Dynamic Mixed Subgrid-Scale Model and Its Application to Turbulent Recirculating Flows," *Physics of Fluids A*, Vol. 5, No. 12, 1993, pp. 3186–3195.

[4]Piomelli, U., "High Reynolds Number Calculations Using the Dynamic Subgrid-Scale Stress Model," *Physics of Fluids A*, Vol. 5, No. 6, 1993, pp. 1484–1490.

[5]Yang, K. S., and Ferziger, J. H., "Large Eddy Simulation of Turbulent Obstacle Flow Using a Dynamic Subgrid-Scale Model," *AIAA Journal*, Vol. 31, No. 8, 1993, pp. 1406–1413.

[6]Vreman, B., Geurts, B., and Kuerten, H., "On the Formulation of the Dynamic Mixed Subgrid-Scale Model," *Physics of Fluids*, Vol. 6, No. 12, 1994, pp. 4057–4059.

[7]Ghosal, S., Lund, T. S., Moin, P., and Akselvoll, K., "A Dynamic Localization Model for Large Eddy Simulation of Turbulent Flows," *Journal of Fluid Mechanics*, Vol. 286, March 1995, pp. 229–255.

[8]Piomelli, U., and Liu, J., "Large Eddy Simulation of Rotating Channel Flows Using a Localized Dynamic Model," *Physics of Fluids*, Vol. 7, No. 4, 1995, pp. 839–848.

[9]Meneveau, C., Lund, T. S., and Cabot, W., "A Lagrangian Dynamic Subgrid-Scale Model of Turbulence," *Journal of Fluid Mechanics*, Vol. 319, July 1996, pp. 353–385.

[10]Wu, X., and Squires, K. D., "Large Eddy Simulation of an Equilibrium Three-Dimensional Turbulent Boundary Layer," *AIAA Journal*, Vol. 35, No. 1, 1997, pp. 67–74.

[11]Wu, X., and Squires, K. D., "Numerical Investigation of the Turbulent Boundary Layer over a Bump," *Journal of Fluid Mechanics*, Vol. 362, May 1998, pp. 229–271.

[12]Balaras, E., Benocci, C., and Piomelli, U., "Two-Layer Approximate Boundary Conditions for Large Eddy Simulations," *AIAA Journal*, Vol. 34, No. 6, 1996, pp. 1111–1119.

[13]Cabot, W., "Near-Wall Models in Large Eddy Simulations of Flow Behind a Backward-Facing Step," *Annual Research Briefs*, Center for Turbulence Research, Stanford Univ., Stanford, CA, 1996, pp. 199–210.

[14]Chapman, D. R., "Computational Aerodynamics Development and Outlook," *AIAA Journal*, Vol. 17, No. 12, 1979, pp. 1293–1313.

[15]Schumann, U., "Subgrid Scale Model for Finite Difference Simulations of Turbulent Flows in Plane Channels and Annuli," *Journal of Computational Physics*, Vol. 18, 1975, pp. 376–404.

[16]Piomelli, U., Ferziger, J., and Moin, P., "New Approximate Boundary Conditions for Large Eddy Simulations of Wall-Bounded Flow," *Physics of Fluids A*, Vol. 1, No. 5, 1989, pp. 1061–1068.

[17]Webster, D., Degraaff, D., and Eaton, J. K., "Turbulence Characteristics of a Boundary Layer over a Two-Dimensional Bump," *Journal of Fluid Mechanics*, Vol. 320, Aug. 1996, pp. 53–69.

[18]Spalart, P. R., and Allmaras, S. R., "A One-Equation Turbulence Model for Aerodynamic Flows," *La Recherche Aerospatiale*, No. 1, 1994, pp. 5–21.

[19]Sotiropoulos, F., and Patel, V. C., "Prediction of Turbulent Flow Through a Transition Duct Using a Second-Moment Closure," *AIAA Journal*, Vol. 32, No. 11, 1994, pp. 2194–2204.

[20]Speziale, C. G., and Xu, X. H., "Towards the Development of Second-Order Closure Models for Nonequilibrium Turbulent Flows," *International Journal of Heat and Fluid Flow*, Vol. 17, No. 3, 1996, pp. 238–244.

[21]Slooten, P. R., and Pope, S. B., "Velocity/Wave-Vector PDF Model Applied to Inhomogeneous Turbulence," *Bulletin of the American Physical Society*, Vol. 41, No. 9, 1996, p. 1798.

[22]Luo, J., and Lakshminarayana, B., "Prediction of Strongly Curved Turbulent Flows with Reynolds Stress Model," *AIAA Journal*, Vol. 35, No. 1, 1997, pp. 91–98.

[23]Durbin, P. A., "Near-Wall Turbulence Closure Modeling Without Damping Functions," *Theoretical Computational Fluid Dynamics*, Vol. 3, No. 1, 1991, pp. 1–13.

[24]Durbin, P. A., "Application of a Near-Wall Turbulence Model to Boundary Layers and Heat Transfer," *International Journal of Heat and Fluid Flow*, Vol. 14, No. 4, 1993, pp. 316–323.

[25]Durbin, P. A., "Separated Flow Computations with the K–ε–v^2 Model," *AIAA Journal*, Vol. 33, No. 4, 1995, pp. 659–664.

[26]Wu, X., and Squires, K. D., "Three-Dimensional Boundary Layers over an Infinite Swept Bump and Free Wing," *Journal of Fluids Engineering*, Vol. 117, Dec. 1995, pp. 605–611.

[27]Rosenfeld, M., Kwak, D., and Vinokur, M., "A Fractional Step Solution Method for the Unsteady Incompressible Navier–Stokes Equations in Generalized Coordinate Systems," *Journal of Computational Physics*, Vol. 94, No. 1, 1991, pp. 102–137.

[28]Choi, H., Moin, P., and Kim, J., "Direct Numerical Simulation of Turbulent Flow over Riblets," *Journal of Fluid Mechanics*, Vol. 255, Oct. 1993, pp. 503–539.

[29]Ghosal, S., and Moin, P., "The Basic Equations for the Large Eddy Simulation of Turbulent Flows in Complex Geometry," *Journal of Computational Physics*, Vol. 118, No. 1, 1995, pp. 24–37.

[30]Lilly, D. K., "A Proposed Modification of the Germano Subgrid-Scale Closure Method," *Physics of Fluids A*, Vol. 4, No. 3, 1992, pp. 633–635.

[31]Spalart, P., "Direct Simulation of a Turbulent Boundary Layer up to $Re_\theta = 1410$," *Journal of Fluid Mechanics*, Vol. 187, Feb. 1988, pp. 61–98.

[32]Lund, T. S., Wu, X., and Squires, K. D., "On the Generation of Turbulent Inflow Conditions for Boundary Layer Simulations," *Annual Research Briefs*, Center for Turbulence Research, Stanford Univ., Stanford, CA, 1996, pp. 281–295.

[33]Lund, T. S., Wu, X., and Squires, K. D., "Generation of Turbulent Inflow Data for Spatially-Developing Boundary Layer Simulations," *Journal of*

Computational Physics, Vol. 140, No. 2, 1998, pp. 233–258.

[34]Werner, H., and Wengle, H., "Large Eddy Simulation of Turbulent Flow over and Around a Cube in a Plate Channel," *Proceedings of the Eighth Symposium on Turbulent Shear Flows*, Technical Univ., Munich, Germany, 1991, pp. 19-4-1–19-4-6.

[35]Baskaran, V., Smits, A. J., and Joubert, P. N., "A Turbulent Flow over a Curved Hill. Part 1. Growth of an Internal Boundary Layer," *Journal of Fluid Mechanics*, Vol. 182, Sept. 1987, pp. 47–83.

[36]Bandyopadhyay, P. R., and Ahmed, A., "Turbulent Boundary Layers Subjected to Multiple Curvatures and Pressure Gradients," *Journal of Fluid Mechanics*, Vol. 246, Jan. 1993, pp. 503–527.

[37]Spalart, P. R., and Watmuff, J. H., "Experimental and Numerical Study of a Turbulent Boundary Layer with Pressure Gradients," *Journal of Fluid Mechanics*, Vol. 249, April 1993, pp. 337–371.

[38]Britter, R. E., Hunt, J. C. R., and Richards, K. J., "A Reynolds Stress Model for Near-Wall Turbulence," *Quarterly Journal of Royal Meteorological Society*, Vol. 107, 1981, pp. 91–110.

[39]Simpson, R. L., "Turbulent Boundary Layer Separation," *Annual Review of Fluid Mechanics*, Vol. 21, 1989, pp. 205–234.

P. R. Bandyopadhyay
Associate Editor

ADVANCED TACTICAL AND STRATEGIC MISSILE GUIDANCE SHORT COURSE

August 20–21, 1998
Arlington, VA

Instructor
Paul Zarchan—C.S. Draper Laboratory

Here's one sequel that's just as good as the original. Picking up where Fundamentals leaves off, this course gives you the foundation in guidance and control technology needed to appreciate the challenges facing interceptor guidance systems. Easy-to-understand numerical examples and computer animations are used to communicate important concepts. The course takes you through a wealth of special problems in tactical and strategic missile guidance. You will learn why common sense often leads to wrong answers when dealing with multiple target problems. And you'll glean invaluable techniques, methods, and tips, like how many Monte Carlo runs you need to accurately calculate the miss distance.

Key Topics
- Advanced problems in tactical and strategic missile guidance.
- Common design pitfalls and their engineering fixes.
- Why ballistic missiles and boosters are challenging targets.
- Optimal guidance laws for improving performance against weaving targets.
- Missile control without moving parts.

Course Outline
Multiple Target Problem • Intercept Point Prediction Error • Boost Phase Estimation • Theater Missile Defense • Weaving Targets • Control System Analysis • Flight Control Systems • The Three Loop Autopilot • Nonlinear Computerized Analysis• Methods That Work • Feedback Linearization • Kalman Filters for Small Miss Distance • The Most Unusual Guidance Method

Course Fee

AIAA Member	$745
Nonmember	$845

Special Reduced Rate!
Register for both Fundamentals and Advanced at the same time and save. The combined fee for the two-course package is:

AIAA Member	$1450
Nonmember	$1600

AIAA

For more information call 800/639-2422; 703/264-7500; Fax 703/264-7551 or visit our Web site at http://www.aiaa.org.